THE JOURNAL OF PHYSICAL CHEMISTRY C

Article

pubs.acs.org/JPCC

High Selectivity of Porous Graphene Electrodes Solely Due to Transport and Pore Depletion Effects

Christian Punckt,[†,‡,§] Michael A. Pope,[†,‡] and Ilhan A. Aksay*[,†]

[†]Department of Chemical and Biological Engineering, Princeton University, Princeton, New Jersey 08544, United States

[‡]Vorbeck Princeton Research Center, Vorbeck Materials Corporation, 11 Deerpark Drive #203, Monmouth Junction, New Jersey 08852, United States

ABSTRACT: We contrast the performance of monolayer electrodes and thin porous film electrodes of highly reduced functionalized graphene to demonstrate that the introduction of electrode porosity gives rise to strong apparent electrocatalytic effects resulting in vastly improved electrode selectivity. This is despite graphene showing no intrinsic advantage over glassy carbon electrodes when used as a monolayer. The simultaneous electro-oxidation of ascorbic acid, dopamine, and uric acid is used as an experimental model electrolyte system. Our results suggest that a large number of reports claiming the superior surface chemistry of carbon nanomaterials as the reason for outstanding electrochemical characteristics should be revisited considering electrode morphology as a significant contributor to the observed behavior. Our experimental results are supported by numerical simulations explaining the porosity-induced electrode selectivity by the dominance of pore depletion over diffusion-limited currents.

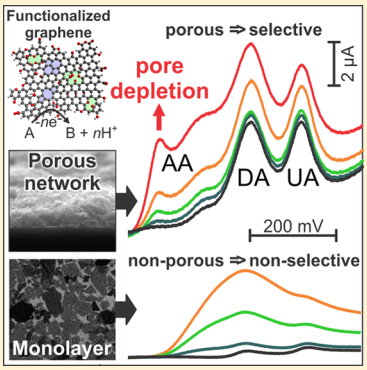

1. INTRODUCTION

When used as electrodes in electroanalytical or electrocatalytic applications, carbon nanomaterials (CNMs) such as carbon nanotubes (CNTs) or graphene are widely regarded superior compared to classical electrode materials such as noble metals or glassy carbon (GC). This has led to a plethora of publications in the field with thousands of articles regarding the electrocatalytic activity of graphene alone, some of which are summarized in recent reviews.[1−9] The outstanding performance of CNMs has mostly been attributed to their unique surface chemistry. However, while it is well established that the particular structure of a carbonaceous surface has a strong impact on its electrochemical behavior, as shown for example by McCreery,[10,11] it should not necessarily be expected that CNMs exhibit vastly different intrinsic properties than GC or graphite powder.[12,13] In the case of graphene, for example, only in a comparably small number of carefully conducted scientific studies has it been shown that certain types of this material indeed exhibit advantageous properties due to their particular structure that cannot be obtained with other forms of carbon. For example, evidence was found for the importance of negatively charged surface functional groups on graphene that facilitate the electro-oxidation of nicotinamide adenine dinucleotide (NADH);[14] the impact of the degree of thermal reduction of graphite oxide (GO) on the general electrochemical activity,[15] the oxidation of nitric oxide,[16] and the catalytic activity toward dye-sensitized solar cell redox mediators[17] was studied in the absence of morphological effects by employing graphene monolayer (ML) electrodes, and the in situ electrochemical reduction of GO electrodes with fixed morphology[18] revealed tunability of its electrochemical properties in a wide range from blocking to highly active. A survey of the current literature, however, suggests that in the majority of cases where superior electrochemical behavior is observed, such behavior could as well be related to electrode morphology[19−22] rather than to extraordinary surface chemistry because electrode morphology is neither controlled nor considered. Surface roughness and electrode porosity (more specifically, pore volume V_p) can contribute significantly or even dominate the electrochemical response measured with CNM-based electrodes.[21−26] While theoretical studies from the groups of Compton[20,27,28] and others[19,29,30] show convincingly that roughness and porosity indeed give rise to effective catalytic behavior, a thorough experimental proof of the relation between morphology and electrochemical performance has been difficult to achieve, since CNM electrodes with negligible roughness and porosity are hard to obtain in practice, and therefore, a one to one comparison of the porous and the nonporous case is challenging.

To alleviate this problem, in a recent experimental study,[26] we examined morphological effects on the performance of porous electrodes made from functionalized graphene sheets (FGSs) which are fabricated by the thermal exfoliation of GO.[31,32] We demonstrated that starting with a FGS ML, which exhibited a behavior practically identical to that of a GC electrode, FGS electrodes with increasing volume of accessible pore space showed increasing apparent electrocatalytic activity and gave rise to "falsified" kinetics. We employed two standard redox probes (RPs), ferro/ferricyanide (FC) and NADH to study both quasi-reversible as well as irreversible kinetics,

Received: July 20, 2014
Revised: September 10, 2014
Published: September 10, 2014

showing that the measured voltammetric data could be understood as a superposition of pore-depletion effects and regular flat electrode response, and we demonstrated ways to deduce intrinsic, surface-specific (rather than morphology-related) performance and redox kinetics from the effective kinetics measured with porous electrodes.

In this study, we demonstrate a very practical aspect of porosity-induced effects of graphene electrodes: the differentiation of electro-oxidation reactions in the simultaneous presence of interfering redox couples. We compare ML and porous drop-cast FGS electrodes, both made with a highly reduced variety of FGSs, and show that while MLs exhibit no intrinsic advantages over GC for use in electroanalysis, effective electrocatalytic behavior and high electrode selectivity (superior to that of GC), i.e., the ability to analytically separate interfering RPs, only arises in case of sufficient accessible electrode pore volume. As a model electrolyte system to study selectivity, we employ the simultaneous electro-oxidation of ascorbic acid (AA), dopamine (DA) and uric acid (UA) which is a popular choice to demonstrate the superior properties of graphene-based[33−41] and various other[42−48] electrode materials. While DA and UA alone are known to give fairly clear voltammetric signals during cyclic or linear sweep voltammetry, due to their tendency to specifically adsorb on the electrode surface (giving rise to a stripping voltammetry-like response),[49,50] the additional presence of high concentrations of AA in this system can swamp the DA and UA signals and prevent any independent quantitation of the three species (interference). GC and FGS ML electrodes show strong interference of AA with DA and UA. However, upon introduction of electrode pore volume, i.e., upon a change of only the electrode morphology, this interference effect can be alleviated. The results obtained with porous electrodes exhibit striking resemblance with published works attributing improved electrode selectivity to surface chemical effects and add further support to the growing community of researchers who acknowledge electrode porosity as a key factor to electroanalytical research.[21,22,24−26,28,29,51−53] Our experiments are accompanied by numerical simulations that help deepen the understanding of the underlying differences in electrolyte transport regimes giving rise to the apparent voltammetric behavior. The findings presented here are applicable to any electrode material exhibiting porosity and will lead researchers both toward a more accurate interpretation of their data as well as to ways to tailor electrode morphology (effective diffusivity, porosity, and thickness) toward optimum sensing and selectivity performance.

2. METHODS

FGS Synthesis and Electrode Fabrication. FGS used in this study was prepared with GO produced by a modified Hummers process described elsewhere[54] using Asbury's 3061 expandable graphite and reagent grade chemicals. To obtain FGSs, about 200 mg of GO was placed in a fused silica tube and dried overnight under a flow of nitrogen gas. The tube was then evacuated and purged with 99.9995% argon three times, evacuated again, and quickly inserted into a 3-zone tube furnace (Lindberg 3M, Thermo Fisher) which had been preheated to a temperature of 1100 °C. The fused silica tube remained inside the furnace for 10 min during which the tube was once purged with argon after 5 min and evacuated again. After removal of the tube from the furnace, the material was allowed to cool to room temperature under a flow of argon. Its degree of reduction was determined by energy dispersive X-ray spectroscopy (INCA x-act, Oxford Instruments, U.K., attached to a Vega 1 scanning electron microscope (SEM), Tescan, Cranberry Twp., PA), which yielded a carbon-to-oxygen ratio (C/O (mol/mol)) of about 60 ± 12 (oxygen content 2.7 ± 0.5%). FGS ML electrodes on gold and HOPG substrates as well as drop-cast FGS electrodes on polished GC substrates were fabricated from dispersions of FGSs (concentration approximately 0.5 mg/mL) in 1,2-dichloroethane (DCE) as described previously.[15] Electrodes with different pore volumes (see below) were fabricated by depositing different amounts of FGS suspension ranging from ∼20 to 200 μL/cm^2 and thus resulting in FGS mass loadings between 10 and 100 μg/cm^2. To block the electrochemical response of the gold substrates, the FGS-coated samples were placed in a 1 mM solution of hexadecanethiol in ethanol for 4 h before use.[15]

Electrochemical Characterization. We conducted all measurements in a custom-made polytetrafluoroethylene (PTFE, Teflon) cell described previously.[15] FGS-coated GC, HOPG or gold substrates served as working electrodes (WEs). A platinum mesh was used as a counter electrode, and the WE potential was measured with respect to a Ag/AgCl reference electrode located 3−4 mm above the WE. Experiments were performed at room temperature with a computer-controlled potentiostat (Model VSP, Biologic, Santa Rosa, CA) using forward feedback to correct for 85% of the Ohmic drop (typically 30−50 Ω) determined by an impedance measurement at 50 kHz, 20 mV amplitude, and at the open circuit voltage (OCV) prior to electrochemical testing. With each electrode, an initial series of cyclic voltammograms (CVs) at various scan rates were recorded in background electrolyte (0.1 M phosphate-buffered saline (PBS) at pH 7.4 with increased KCl concentration of 1 M to minimize ohmic drops) to determine capacitive background currents. This was followed by a series of CVs in FC electrolyte containing 2.5 mM FC in 0.1 M phosphate-buffered saline (PBS) at pH 7.4 with increased KCl concentration of 1 M. After careful rinsing in deionized (DI) water, the electrodes were then used to record CVs and linear sweep voltammograms (LSVs) in PBS electrolytes containing AA, DA, and UA at different concentrations. For the measurements with AA, DA, and UA, no ohmic drop compensation was applied since compensation might cause minute improvements in apparent selectivity. All chemicals were reagent grade and electrolytes were prepared freshly at the day of the experiment with DI water of greater than 18 MΩ·cm resistivity.

Evaluation of Electrode Roughness, Porosity, Pore Volume, and Average Pore Size. As in our previous studies, we employed the FC redox couple to determine electrode porosity.[16,26] To this end, we first determined the rate of heterogeneous electron transfer k_0 of FC on FGSs and the intrinsic capacitance C_{INT} from CV data with FGS ML electrodes (Figure 1a). As discussed previously,[26] the individual ML electrodes each exhibited slightly different roughness and minute amounts of porosity, as is evident from a plot of the separation between oxidation and reduction peak E_{pp} on the potential axis as a function of the previously defined phenomenological porosity or roughness factor[23]

$$P = \frac{\alpha(2000\ \mathrm{mV/s})}{\alpha(50\ \mathrm{mV/s})} \quad (1)$$

dx.doi.org/10.1021/jp507238u | J. Phys. Chem. C 2014, 118, 22635−22642

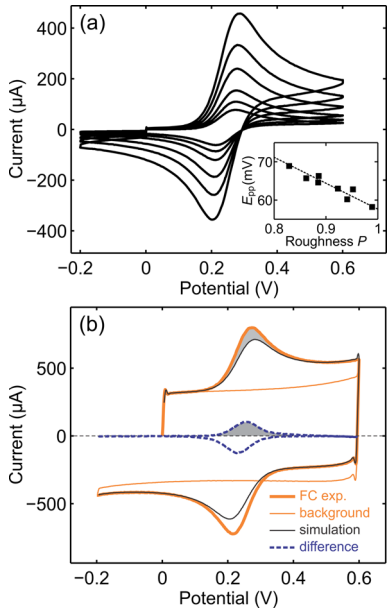

Figure 1. Electrode characterization with FC redox couple. (a) CVs of FC obtained with FGS-ML electrode at scan rates between 0.05 and 2 V/s. The inset shows the peak-to-peak separation as a function of the roughness factor P for all ML electrodes tested. (b) Example for porosity analysis using the FC RP with a drop-cast FGS electrode.[26]

where $\alpha = I_{forw}/\sqrt{\nu}$ represents the ratio of the oxidation peak current I_{forw} and the square root of the corresponding voltage scan rate ν (inset of Figure 1a). Interpolating the data to a value of $P = 0.9$ (taking into account the quasi-reversible nature of the reaction which yields $P \approx 0.9$ for polished GC as well)[26,55] gave a reliable estimate of $E_{pp} = 64.4$ mV from which $k_0 = 3.3 \times 10^{-2}$ cm/s could be calculated in a straightforward manner.[26,55] Analysis of the capacitive background current (containing contributions from pseudocapacitance) yielded a value of $C_{INT} \approx 40\ \mu F/cm^2$.

In the next step, the pore volume of drop-cast FGS electrodes made from the same batch of FGS material could be determined through computer-aided analysis of the data (Figure 1b).[26] We added the CV measured at $\nu = 1$ V/s with the porous electrode in background electrolyte to the simulated CV of a flat electrode with corresponding projected surface area A_0 in FC electrolyte. This curve was then subtracted from the corresponding measured CV in FC electrolyte. The area underneath the difference curve (shaded gray area in Figure 1b) is proportional to the number of ferrocyanide molecules contained within the pore space of the electrode. Knowing the FC concentration, we obtained the volume of the accessible pore space V_p for each electrode tested ($V_p = 111$ nL in the example shown in Figure 1b). From the capacitive background current, the approximate accessible electrode surface area A could be estimated. For the result shown in Figure 1b, we obtained $A = 22.5\ cm^2$. Assuming slit-like pores with equal size, we defined an average pore size $s = V_p/A$,[26] yielding $s \approx 50$ nm for the example shown.

Numerical Simulations. CVs were simulated as detailed previously.[26] Electrolyte transport through the bulk electrolyte was assumed to take place through 1-dimensional semi-infinite diffusion, and electrochemical kinetics were defined by the Butler–Volmer equation:[55].

$$I = nFA_0k_0\left(C_{Red}\exp\left\{\frac{nF\tilde{E}}{RT}\right\} - C_{Ox}\exp\left\{\frac{-nF\tilde{E}}{RT}\right\}\right) \quad (2)$$

Here, I denotes the net redox current, n is the number of electrons involved in the reaction, F is Faraday's constant; C_{Red} and C_{Ox} are the concentrations of reduced and oxidized redox species at the electrode/electrolyte interface, respectively; $\tilde{E} = E - E_0$ is the overpotential, i.e., the difference between applied potential E and equilibrium potential E_0; R is the universal gas constant, and T is the absolute temperature (298.15 K). To simulate the CVs of FC, the reduced and oxidized species in the bulk electrolyte were assigned diffusion coefficients of $D_{Red} = 6.3 \times 10^{-5}\ cm^2/s$ and $D_{Ox} = 7.6 \times 10^{-5}\ cm^2/s$.[55] The rate of heterogeneous electron transfer was set to the value determined experimentally ($k_0 = 3.5 \times 10^{-2}$ cm/s). The simulations were initialized by setting the concentrations of the reduced and the oxidized species to values of 2.5 and 0 mM, respectively. LSVs mimicking the simultaneous detection of interfering RPs were simulated using the following parameters: $k_0 = 10^{-5}$ cm/s, $D_0 = D_{Red} = D_{Ox} = 6.3 \times 10^{-5}\ cm^2/s$.

The transport within porous electrodes was simulated using effective diffusivities D_{eff},[26,56−58] i.e., instead of explicitly taking into account the complex 3-dimensional structure of the electrode, we described ion transport within the tortuous pore space defined by the graphene sheets simply through the impact of porosity and tortuosity on the effective transport of ions on a scale much greater than the individual FGSs. D_{eff} was varied between D_0 (theoretical case of negligible impact of electrode porosity and tortuosity on transport) and $D_0/50$ (transport strongly impeded). Within the porous electrode, we assigned an effective surface area $A_{pore} = A_0\Delta x/s$ to each volume element Δx depending on pore size s and A_0. A_{pore} enters eq 2 as surface area to calculate the contribution of each volume element within the porous electrode to the total redox current.

3. RESULTS AND DISCUSSION

Experimental Work. In Figure 2, we display CVs and LSVs obtained with FGS ML electrodes and drop-cast electrodes in comparison to GC in an electrolyte containing AA, DA, and UA. In experiments with the ML electrodes (Figure 2a), we observe only minute differences between the FGS and the GC electrode. Both for FGS ML and for GC, the three oxidation peaks overlap, and in particular the AA peak lies so close to the DA peak that it is only noticeable as a shoulder on the DA peak. The comparably clear separation of the DA and UA peaks is due to the fact that DA and UA specifically adsorb on the electrodes,[49] giving rise to a high peak current followed by quick drop-off similar to the electrochemical response in case of thin-film diffusion. The different height ratios of the DA and UA peaks for FGSs and GC suggest that DA and UA might have slightly different adsorption kinetics on the two materials since the ratio is mostly determined by the initial rate of adsorption while DA and UA compete for adsorption sites.

To study the impact of AA as an interferent, we conducted measurements with fixed concentrations of DA and UA and varying AA concentration (Figure 2b). For our flat electrodes, the addition of increasing amounts of AA quickly swamps the DA and UA peaks (as shown for GC in the Figure). At an AA concentration of 100 μM, the contributions of the three redox species to the oxidation current can hardly be distinguished. On the other hand, the interfering effect of AA can be eliminated (Figure 2b) using drop-cast FGS electrodes of increasing pore

dx.doi.org/10.1021/jp507238u | J. Phys. Chem. C 2014, 118, 22635−22642

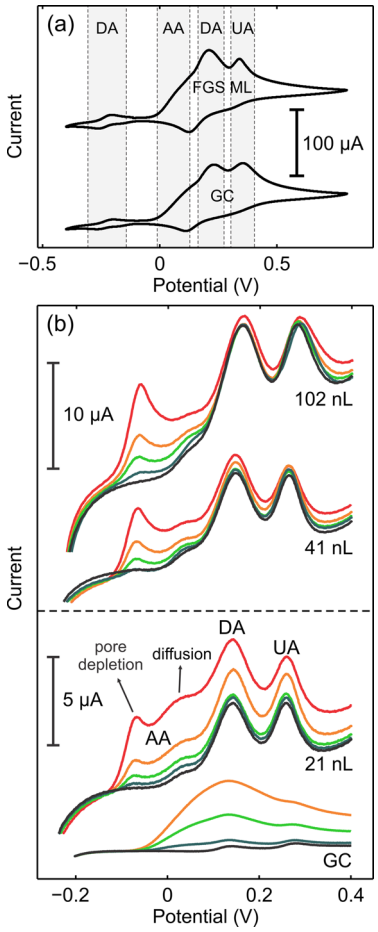

Figure 2. Electrochemical response obtained with electrolytes containing mixtures of AA, DA, and UA in PBS. (a) CVs obtained with FGS-ML and bare GC electrodes at 100 mV/s scan rate, 0.1 M PBS electrolyte with 100 μM AA, 100 μM DA and 100 μM UA. (b) Comparison of LSVs obtained with drop-cast FGS electrodes (pore volumes as indicated) in comparison to bare GC at 50 mV/s scan rate. A 0.1 M PBS electrolyte with 3 μM DA and 3 μM UA. AA is present at concentrations of 0 (black curve), 20 (dark green), 50 (light green), 100 (orange), and 200 μM (red). For GC, the maximum AA concentration is 100 μM.

volume: With a total accessible pore volume of V_p = 21 nL, the AA oxidation response moves to smaller potentials and splits into two separate peaks which we attribute to a thin-film diffusion response due to pore depletion (peak around −80 mV vs Ag/AgCl) and the effective diffusion-limited response of the electrode (peak around +50 mV vs Ag/AgCl) due to an increase of the number of electroactive sites per geometric surface area (effective catalytic activity) as indicated in the Figure.[26] At the same time, the magnitude of the DA and UA peaks is greatly increased compared to the flat electrode due to the large amount of electrode surface area available for adsorption. Consequently, the addition of AA up to 50 μM has little impact on the value of the DA peak current. Increasing the pore volume to 41 nL results in an amplification of the observed changes: The pore depletion-related AA oxidation peak now dominates over the diffusion-limited AA response, while DA and UA peaks further increase in magnitude and show less dependence on the presence of AA compared to the 21 nL case. At the highest pore volume of V_p = 102 nL, the general trends persist, with the exception that all peaks are slightly shifted toward higher potential. We attribute this to an increased contribution of ohmic potential drop within the thick FGS film.

In summary, we contend that the observed benefits of high pore volume are due to two factors: (i) The increased pore volume gives rise to the emergence of pore depletion effects as discussed in our recent work.[26] The corresponding feature in the LSV is a thin-film diffusion-like response shifted to significantly smaller overpotentials. This effect results in the emergence of a new AA peak around a potential of −80 mV vs Ag/AgCl upon introduction of electrode porosity and can also be expected to contribute to the increased DA and UA oxidation currents. (ii) Electrode porosity increases the amount of available total electrode surface area. The 21 nL electrode whose response is shown in Figure 2b, for example, exhibits an accessible surface area of A = 4.3 cm^2 while having a geometric surface area of A_0 = 0.22 cm^2. This causes an effective electrocatalytic effect for AA, as it can diffuse from the bulk electrolyte into the porous electrode and therefore can access an increased number of electrochemically active sites. Furthermore, the increased surface area allows for adsorption of similarly increased amounts of DA and UA, which consequently results in a corresponding increase of oxidation current by more than 1 order of magnitude. In combination, these two factors reduce interference between AA and DA (or UA): By the time the greatly enhanced DA oxidation peak is measured during voltammetry, the concentration of non-oxidized AA within the porous electrode is close to zero, while at the same time the diffusion-limited current due to transport of AA from the bulk electrolyte has decayed to a negligible value. The operation of an electrochemical sensor electrode in this fashion bears similarity to stripping voltammetry, which has been pointed out in previous studies.[25,28,29]

Numerical Simulations. To support our interpretation of the experimental data, we conducted numerical simulations of LSVs with porous electrodes of different thickness, i.e., different pore volume, and different pore size in the presence of three hypothetical RPs (RP I, II, and III) with irreversible kinetics (k_0 = 10^{-5} cm/s) and equilibrium potentials of 0, 150, and 300 mV based on the procedure detailed in ref 26. The results are shown in Figure 3. With increasing electrode thickness (Figure 3a), the initially convoluted oxidation peaks seen with the flat electrode shift to smaller potentials, become increasingly well separated, and increase in magnitude. Decreasing pore size (Figure 3b) amplifies this effect. Since in our simulations adsorption is not taken into account, all redox peaks are subject to the same shifts and magnitude changes. Nonetheless, we see that there is a qualitative agreement between the simulations and the experimental results. It should be emphasized that the rate of heterogeneous electron transfer is not changed in this series of simulations. Therefore, the observed effects are indeed all related solely to changes in electrode morphology.

To better understand these results, we varied the effective diffusivity within the porous electrode as shown in Figure 4. Much to our surprise, the effect of varying D_{eff} is close to negligible in the simulated combined response to all three RPs (Figure 4a). The only noticeable effect is the emergence of an additional redox peak at around 500 mV for $D_{eff} = D_0/50$ which is absent for $D_{eff} = D_0$. Studying the oxidation current due to RP I alone sheds more light on this observation (Figure 4b): For a low value of D_{eff}, two oxidation peaks are observed, while for $D_{eff} = D_0$, only one oxidation peak emerges. This can be

dx.doi.org/10.1021/jp507238u | J. Phys. Chem. C 2014, 118, 22635−22642

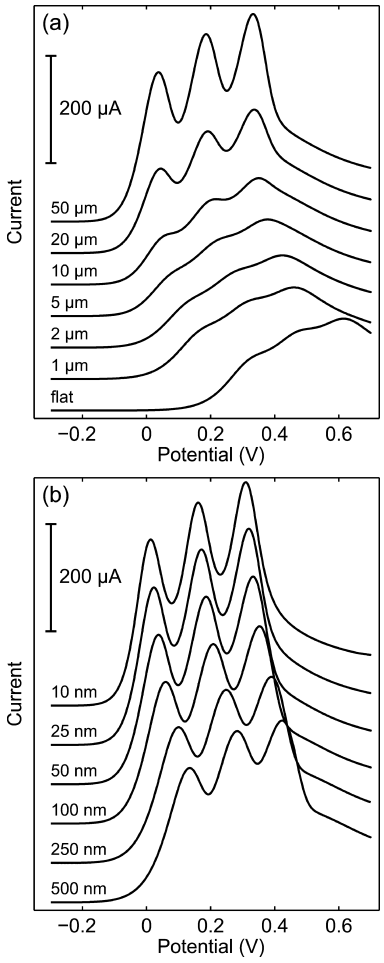

Figure 3. Numerical simulation of LSVs on porous electrodes. Impact of (a) thickness and (b) pore size of the porous electrode film on LSVs obtained during the simultaneous electro-oxidation of RP I–III. The pore size in (a) is 50 nm and the film thickness in (b) is 50 μm.

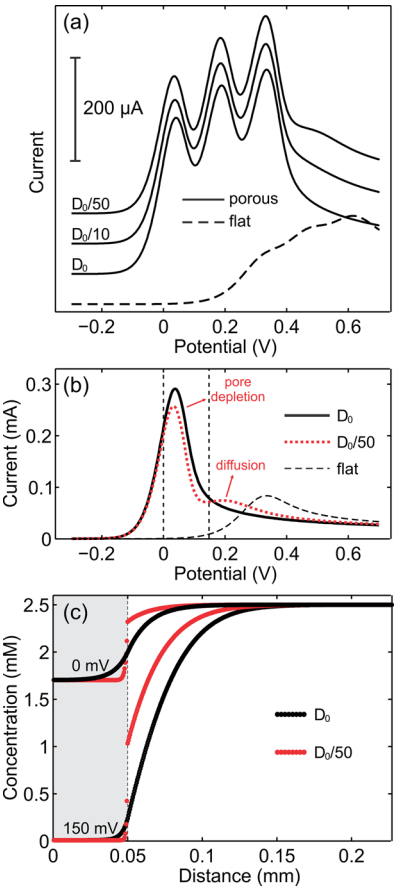

Figure 4. Numerical simulation of LSVs on porous electrodes. (a) LSVs obtained for simultaneous presence of RP I–III with porous electrodes exhibiting different effective diffusivity in comparison to LSV with flat electrode. (b) LSV with single redox couple (E_0 = 0 V), comparison of a flat electrode with porous electrodes of 50 μm thickness and different effective diffusivities. (c) Concentration profiles of reduced species corresponding to porous electrode responses shown in (b) at indicated potentials.

explained considering the temporal evolution of the RP concentration throughout the system (Figure 4c):. In the case of low effective diffusivity, the porous electrode becomes depleted of RP I before the concentration gradient in the bulk electrolyte reaches its maximum. Therefore, the thin film diffusion-like pore depletion peak (in case of the chosen simulation parameters occurring near E_0) is separated from the peak due to semi-infinite diffusive transport (diffusion-limited peak) associated with the maximum in concentration gradient within the bulk electrolyte. Due to a small amount of diffusion still occurring within the porous film adjacent to the bulk electrolyte, the diffusion-limited peak is shifted to smaller potentials compared to the flat electrode response due to the increased effective reactive surface area.

With $D_{eff} = D_0$, RP I is replenished from the bulk electrolyte within a significant fraction of the porous electrode film. This results in a stronger effective catalytic effect, shifting the semi-infinite diffusion-related peak so far to smaller potentials that it overlaps with the pore depletion peak. The maximum of the concentration gradient in the bulk electrolyte occurs approximately at the same time the porous film is fully depleted. We note that the double oxidation peak seen in our simulations for $D_{eff} = D_0/50$ is reminiscent of the AA double peak observed experimentally (Figure 2b) which leads us to conclude that AA diffusion within the FGS electrode is strongly impeded.

To illustrate the effect of porosity on interference between RP I and II, we conducted simulations with varying concentration of RP I, while the concentrations of RP II and III were kept constant (Figure 5). Again, the simulations correspond qualitatively to our experimental observations that the oxidation current due to RP I (AA) has a lesser impact on the current measured at the locations of the oxidation peaks of RP II (DA) and III (UA). However, the effect is much less pronounced in our simulations than in the experiments. This can be explained by considering that in the simulation the oxidation peaks for all three RPs shift, while in the experiments the oxidation peaks of DA and UA remain at approximately the same potential as they are due to the oxidation of adsorbed species. This results in an effective peak separation of more than 200 mV between the AA depletion peak and the oxidation peak due to adsorbed DA in the experiment, while in the simulation the separation of voltammetric features due to RP I and II always remains 150 mV. However, this consideration illustrates that electrode porosity can improve selectivity even in systems where specific adsorption does not occur.

dx.doi.org/10.1021/jp507238u | J. Phys. Chem. C 2014, 118, 22635–22642

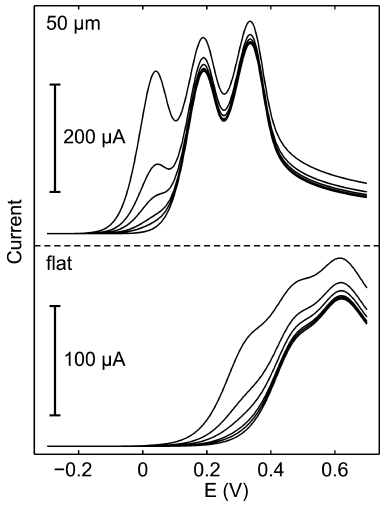

Figure 5. Simulated LSVs for simultaneous electro-oxidation of RP I–III with varying concentration of RP I. Comparison of porous electrode with 50 μm thickness and $D_{eff} = 0.1 \cdot D_0$ with flat electrode. The concentrations of RP I are 0, 0.1, 0.2, 0.5, 1.0, and 2.5 mM.

4. CONCLUSIONS

By employing FGSs with intrinsic electrochemical characteristics almost identical to those of GC, we have demonstrated that effective electrocatalysis and excellent suppression of RP interference can be achieved solely by introducing electrode porosity. This has important implications for existing studies on the proposed impact of FGS structure on electroanalytical performance of FGS electrodes, since it suggests that in cases where electrode morphology was not accounted for, observations might to a large extent or even completely be due to the transport effects described above. Additionally, it should be pointed out that for materials that indeed act as electrocatalysts, including chemically modified or decorated graphene, the additional design of a suitable porous electrode architecture will have an amplifying effect and increase catalytic activity. Moreover, the increasing dominance of the pore depletion current with increasing pore volume causes a significant narrowing of the redox peaks (characteristic for thin-film diffusion)[28,55] which improves selectivity and minimizes interference regardless of the intrinsic rate of electron transfer. For fast electrochemical reactions, this implies that although their effective rate of electron transport might not be increased significantly, tailoring an electrode's pore-size and pore-volume can be used as a means to better separate redox peaks of interfering species in order to improve selectivity.

AUTHOR INFORMATION

Corresponding Author

*E-mail: iaksay@princeton.edu.

Present Address

[§]Institute of Nanotechnology, Karlsruhe Institute of Technology, D-76344 Eggenstein-Leopoldshafen, Germany.

Author Contributions

FGS ML electrodes were prepared by M.A.P., remaining procedures and experiments were conducted by C.P. The manuscript was written through contributions of all authors and all authors have given approval to the final version of the manuscript.

Notes

The authors declare no competing financial interest.

ACKNOWLEDGMENTS

This work was supported by the Pacific Northwest National Laboratory (operated for the United States Department of Energy by Battelle) under Grant Number DE-AC05-76RL01830 and by the Small Business Innovation Research program of the National Science Foundation under Grant Number IIP-1142890.

REFERENCES

(1) Chen, D.; Tang, L.; Li, J. Graphene-Based Materials in Electrochemistry. *Chem. Soc. Rev.* **2010**, *39*, 3157–3180.
(2) Pumera, M.; Ambrosi, A.; Bonanni, A.; Chng, E. L. K.; Poh, H. L. Graphene for Electrochemical Sensing and Biosensing. *TrAC, Trends Anal. Chem.* **2010**, *29*, 954–965.
(3) Shao, Y. Y.; Wang, J.; Wu, H.; Liu, J.; Aksay, I. A.; Lin, Y. H. Graphene Based Electrochemical Sensors and Biosensors: A Review. *Electroanalysis* **2010**, *22*, 1027–1036.
(4) Kuila, T.; Bose, S.; Khanra, P.; Mishra, A. K.; Kim, N. H.; Lee, J. H. Recent Advances in Graphene-Based Biosensors. *Biosens. Bioelectron.* **2011**, *26*, 4637–4648.
(5) Gan, T.; Hu, S. Electrochemical Sensors Based on Graphene Materials. *Microchim. Acta* **2011**, *175*, 1–19.
(6) Machado, B. F.; Serp, P. Graphene-Based Materials for Catalysis. *Catal. Sci. Technol.* **2012**, *2*, 54–75.
(7) Huang, C.; Li, C.; Shi, G. Graphene Based Catalysts. *Energy Environ. Sci.* **2012**, *5*, 8848–8868.
(8) Brownson, D. A. C.; Kampouris, D. K.; Banks, C. E. Graphene Electrochemistry: Fundamental Concepts through to Prominent Applications. *Chem. Soc. Rev.* **2012**, *41*, 6944–6976.
(9) Hur, S. H.; Park, J.-N. Graphene and Its Application in Fuel Cell Catalysis: A Review. *Asia–Pac. J. Chem. Eng.* **2013**, *8*, 218–233.
(10) Ranganathan, S.; McCreery, R. L. Electroanalytical Performance of Carbon Films with near-Atomic Flatness. *Anal. Chem.* **2001**, *73*, 893–900.
(11) McCreery, R. L. Advanced Carbon Electrode Materials for Molecular Electrochemistry. *Chem. Rev.* **2008**, *108*, 2646–2687.
(12) Moore, R. R.; Banks, C. E.; Compton, R. G. Basal Plane Pyrolytic Graphite Modified Electrodes: Comparison of Carbon Nanotubes and Graphite Powder as Electrocatalysts. *Anal. Chem.* **2004**, *76*, 2677–2682.
(13) Pumera, M. Voltammetry of Carbon Nanotubes and Graphenes: Excitement, Disappointment, and Reality. *Chem. Rec.* **2012**, *12*, 201–213.
(14) Pumera, M.; Scipioni, R.; Iwai, H.; Ohno, T.; Miyahara, Y.; Boero, M. A Mechanism of Adsorption of Beta-Nicotinamide Adenine Dinucleotide on Graphene Sheets: Experiment and Theory. *Chem.—Eur. J.* **2009**, *15*, 10851–10856.
(15) Pope, M. A.; Punckt, C.; Aksay, I. A. Intrinsic Capacitance and Redox Activity of Functionalized Graphene Sheets. *J. Phys. Chem. C* **2011**, *115*, 20326–20334.
(16) Liu, Y. M.; Punckt, C.; Pope, M. A.; Gelperin, A.; Aksay, I. A. Electrochemical Sensing of Nitric Oxide with Functionalized Graphene Electrodes. *ACS Appl. Mater. Interface* **2013**, *5*, 12624–12630.
(17) Roy-Mayhew, J. D. *Functionalized Graphene Sheets in Dye-Sensitized Solar Cell Counter Electrodes*. Ph.D. Dissertation, Princeton University, Princeton, NJ, 2013.
(18) Ambrosi, A.; Pumera, M. Precise Tuning of Surface Composition and Electron-Transfer Properties of Graphene Oxide Films through Electroreduction. *Chem.—Eur. J.* **2013**, *19*, 4748–4753.
(19) Zuo, X. B.; Xu, C. S.; Xin, H. W. Simulation of Voltammogram on Rough Electrode. *Electrochim. Acta* **1997**, *42*, 2555–2558.
(20) Menshykau, D.; Compton, R. G. The Influence of Electrode Porosity on Diffusional Cyclic Voltammetry. *Electroanalysis* **2008**, *20*, 2387–2394.

(21) Menshykau, D.; Streeter, I.; Compton, R. G. Influence of Electrode Roughness on Cyclic Voltammetry. *J. Phys. Chem. C* **2008**, *112*, 14428−14438.
(22) Keeley, G. P.; Lyons, M. E. G. The Effects of Thin Layer Diffusion at Glassy Carbon Electrodes Modified with Porous Films of Single-Walled Carbon Nanotubes. *Int. J. Electrochem. Sci.* **2009**, *4*, 794−809.
(23) Punckt, C.; Pope, M. A.; Liu, J.; Lin, Y. H.; Aksay, I. A. Electrochemical Performance of Graphene as Effected by Electrode Porosity and Graphene Functionalization. *Electroanalysis* **2010**, *22*, 2834−2841.
(24) Henstridge, M. C.; Dickinson, E. J. F.; Compton, R. G. Mass Transport to and within Porous Electrodes. Linear Sweep Voltammetry and the Effects of Pore Size: The Prediction of Double Peaks for a Single Electrode Process. *Russ. J. Electrochem.* **2012**, *48*, 629−635.
(25) Kutluay, A.; Aslanoglu, M. Modification of Electrodes Using Conductive Porous Layers to Confer Selectivity for the Voltammetric Detection of Paracetamol in the Presence of Ascorbic Acid, Dopamine and Uric Acid. *Sens. Actuators, B* **2013**, *185*, 398−404.
(26) Punckt, C.; Pope, M. A.; Aksay, I. A. On the Electrochemical Response of Porous Functionalized Graphene Electrodes. *J. Phys. Chem. C* **2013**, *117*, 16076−16086.
(27) Menshykau, D.; Compton, R. G. Influence of Electrode Roughness on Stripping Voltammetry: Mathematical Modeling and Numerical Simulation. *J. Phys. Chem. C* **2009**, *113*, 15602−15620.
(28) Henstridge, M. C.; Dickinson, E. J. F.; Aslanoglu, M.; Batchelor-McAuley, C.; Compton, R. G. Voltammetric Selectivity Conferred by the Modification of Electrodes Using Conductive Porous Layers or Films: The Oxidation of Dopamine on Glassy Carbon Electrodes Modified with Multiwalled Carbon Nanotubes. *Sens. Actuators, B* **2010**, *145*, 417−427.
(29) Laborda, E.; Molina, A.; Martinez-Ortiz, F.; Compton, R. G. Electrode Modification Using Porous Layers. Maximising the Analytical Response by Choosing the Most Suitable Voltammetry: Differential Pulse Vs Square Wave Vs Linear Sweep Voltammetry. *Electrochim. Acta* **2012**, *73*, 3−9.
(30) Menzel, N.; Ortel, E.; Kraehnert, R.; Strasser, P. Electrocatalysis Using Porous Nanostructured Materials. *ChemPhysChem* **2012**, *13*, 1385−1394.
(31) Schniepp, H. C.; Li, J. L.; McAllister, M. J.; Sai, H.; Herrera-Alonso, M.; Adamson, D. H.; Prud'homme, R. K.; Car, R.; Saville, D. A.; Aksay, I. A. Functionalized Single Graphene Sheets Derived from Splitting Graphite Oxide. *J. Phys. Chem. B* **2006**, *110*, 8535−8539.
(32) McAllister, M. J.; Li, J. L.; Adamson, D. H.; Schniepp, H. C.; Abdala, A. A.; Liu, J.; Herrera-Alonso, M.; Milius, D. L.; Car, R.; Prud'homme, R. K.; et al. Single Sheet Functionalized Graphene by Oxidation and Thermal Expansion of Graphite. *Chem. Mater.* **2007**, *19*, 4396−4404.
(33) Mallesha, M.; Manjunatha, R.; Nethravathi, C.; Suresh, G. S.; Rajamathi, M.; Melo, J. S.; Venkatesha, T. V. Functionalized-Graphene Modified Graphite Electrode for the Selective Determination of Dopamine in Presence of Uric Acid and Ascorbic Acid. *Bioelectrochemistry* **2011**, *81*, 104−108.
(34) Chao, M.; Ma, X.; Li, X. Graphene-Modified Electrode for the Selective Determination of Uric Acid under Coexistence of Dopamine and Ascorbic Acid. *Int. J. Electrochem. Sci.* **2012**, *7*, 2201−2213.
(35) Ma, X.; Chao, M.; Wang, Z. Electrochemical Detection of Dopamine in the Presence of Epinephrine, Uric Acid and Ascorbic Acid Using a Graphene-Modified Electrode. *Anal. Methods* **2012**, *4*, 1687−1692.
(36) Ping, J.; Wu, J.; Wang, Y.; Ying, Y. Simultaneous Determination of Ascorbic Acid, Dopamine and Uric Acid Using High-Performance Screen-Printed Graphene Electrode. *Biosens. Bioelectron.* **2012**, *34*, 70−76.
(37) Sheng, Z. H.; Zheng, X. Q.; Xu, J. Y.; Bao, W. J.; Wang, F. B.; Xia, X. H. Electrochemical Sensor Based on Nitrogen Doped Graphene: Simultaneous Determination of Ascorbic Acid, Dopamine and Uric Acid. *Biosens. Bioelectron.* **2012**, *34*, 125−131.
(38) Gao, F.; Cai, X.; Wang, X.; Gao, C.; Liu, S.; Gao, F.; Wang, Q. Highly Sensitive and Selective Detection of Dopamine in the Presence of Ascorbic Acid at Graphene Oxide Modified Electrode. *Sens. Actuators, B* **2013**, *186*, 380−387.
(39) Kaur, B.; Pandiyan, T.; Satpati, B.; Srivastava, R. Simultaneous and Sensitive Determination of Ascorbic Acid, Dopamine, Uric Acid, and Tryptophan with Silver Nanoparticles-Decorated Reduced Graphene Oxide Modified Electrode. *Colloid Surf., B* **2013**, *111*, 97−106.
(40) Li, S.-M.; Yang, S.-Y.; Wang, Y.-S.; Lien, C.-H.; Tien, H.-W.; Hsiao, S.-T.; Liao, W.-H.; Tsai, H.-P.; Chang, C.-L.; Ma, C.-C. M.; et al. Controllable Synthesis of Nitrogen-Doped Graphene and Its Effect on the Simultaneous Electrochemical Determination of Ascorbic Acid, Dopamine, and Uric Acid. *Carbon* **2013**, *59*, 418−429.
(41) Yu, Y.; Chen, Z.; Zhang, B.; Li, X.; Pan, J. Selective and Sensitive Determination of Uric Acid in the Presence of Ascorbic Acid and Dopamine by Pdda Functionalized Graphene/Graphite Composite Electrode. *Talanta* **2013**, *112*, 31−36.
(42) Ramesh, P.; Sampath, S. Selective Determination of Uric Acid in Presence of Ascorbic Acid and Dopamine at Neutral pH Using Exfoliated Graphite Electrodes. *Electroanalysis* **2004**, *16*, 866−869.
(43) Liu, A.; Honma, I.; Zhou, H. Simultaneous Voltammetric Detection of Dopamine and Uric Acid at Their Physiological Level in the Presence of Ascorbic Acid Using Poly(acrylic acid)-Multiwalled Carbon-Nanotube Composite-Covered Glassy-Carbon Electrode. *Biosens. Bioelectron.* **2007**, *23*, 74−80.
(44) Zhu, S.; Li, H.; Niu, W.; Xu, G. Simultaneous Electrochemical Determination of Uric Acid, Dopamine, and Ascorbic Acid at Single-Walled Carbon Nanohorn Modified Glassy Carbon Electrode. *Biosens. Bioelectron.* **2009**, *25*, 940−943.
(45) Huang, S.-H.; Liao, H.-H.; Chen, D.-H. Simultaneous Determination of Norepinephrine, Uric Acid, and Ascorbic Acid at a Screen Printed Carbon Electrode Modified with Polyacrylic Acid-Coated Multi-Wall Carbon Nanotubes. *Biosens. Bioelectron.* **2010**, *25*, 2351−2355.
(46) Chitravathi, S.; Swamy, B. E. K.; Mamatha, G. P.; Sherigara, B. S. Simultaneous Electrochemical Determination of Dopamine and Ascorbic Acid Using Poly (L-Serine) Modified Carbon Paste Electrode. *J. Mol. Liq.* **2011**, *160*, 193−199.
(47) Zhang, W.; Yuan, R.; Chai, Y.-Q.; Zhang, Y.; Chen, S.-H. A Simple Strategy Based on Lanthanum-Multiwalled Carbon Nanotube Nanocomposites for Simultaneous Determination of Ascorbic Acid, Dopamine, Uric Acid and Nitrite. *Sens. Actuators, B* **2012**, *166*, 601−607.
(48) Zhang, W.; Chai, Y.; Yuan, R.; Han, J.; Chen, S. Deposited Gold Nanocrystals Enhanced Porous Ptca-Cys Layer for Simultaneous Detection of Ascorbic Acid, Dopamine and Uric Acid. *Sens. Actuators, B* **2013**, *183*, 157−162.
(49) DuVall, S. H.; McCreery, R. L. Self-Catalysis by Catechols and Quinones During Heterogeneous Electron Transfer at Carbon Electrodes. *J. Am. Chem. Soc.* **2000**, *122*, 6759−6764.
(50) Ernst, H.; Knoll, M. Electrochemical Characterisation of Uric Acid and Ascorbic Acid at a Platinum Electrode. *Anal. Chim. Acta* **2001**, *449*, 129−134.
(51) Szamocki, R.; Velichko, A.; Holzapfel, C.; Mucklich, F.; Ravaine, S.; Garrigue, P.; Sojic, N.; Hempelmann, R.; Kuhn, A. Macroporous Ultramicroelectrodes for Improved Electroanalytical Measurements. *Anal. Chem.* **2007**, *79*, 533−539.
(52) Niu, X.; Lan, M.; Zhao, H.; Chen, C. Well-Dispersed Pt Cubes on Porous Cu Foam: High-Performance Catalysts for the Electrochemical Oxidation of Glucose in Neutral Media. *Chem.—Eur. J.* **2013**, *19*, 9534−9541.
(53) Niu, X.; Zhao, H.; Chen, C.; Lan, M. Enhancing the Electrocatalytic Activity of Pt-Pd Catalysts by Introducing Porous Architectures. *Chem. Catal. Chem.* **2013**, *5*, 1416−1425.
(54) Marcano, D. C.; Kosynkin, D. V.; Berlin, J. M.; Sinitskii, A.; Sun, Z. Z.; Slesarev, A.; Alemany, L. B.; Lu, W.; Tour, J. M. Improved Synthesis of Graphene Oxide. *ACS Nano* **2010**, *4*, 4806−4814.

(55) Bard, J. A.; Faulkner, L. R. *Electrochemical Methods*, 2nd ed.; John Wiley & Sons: New York, 2001.
(56) Newman, J. S.; Tobias, C. W. Theoretical Analysis of Current Distribution in Porous Electrodes. *J. Electrochem. Soc.* **1962**, *109*, 1183−1191.
(57) Newman, J.; Tiedemann, W. Porous-Electrode Theory with Battery Applications. *AIChE J.* **1975**, *21*, 25−41.
(58) Akanni, K. A.; Evans, J. W. Effective Transport-Coefficients in Heterogeneous Media. *Chem. Eng. Sci.* **1987**, *42*, 1945−1954.